ACS APPLIED ENERGY MATERIALS

Open Access

www.acsaem.org

Article

Tuning Phase Composition and Electrocatalytic Activity via Nickel Doping in Magnetron-Sputtered Iron Oxide Coatings

Ieva Barauskiene,* Alexandre C. Bastos, Filipe M. L. Figueiredo, and Giedrius Laukaitis

Cite This: https://doi.org/10.1021/acsaem.6c01330

Read Online

ACCESS | Metrics & More | Article Recommendations | Supporting Information

ABSTRACT: This paper reports a study of Nickel-doped iron oxide coatings deposited on AISI 304 stainless steel via reactive magnetron sputtering using hematite and metallic nickel targets in an Ar/O_2 atmosphere (70/30). The Ni target power varies between 25 and 60 W to control Ni incorporation and investigate its effect on phase transformations within the iron oxide matrix. Structural analysis demonstrates that Ni addition strongly influences both the degree of amorphization and the phase composition of the deposited coatings. Electrocatalytic evaluation toward the oxygen evolution reaction (OER) reveals no direct correlation between Ni concentration and catalytic performance. Instead, the results indicate that the phase composition and the interplay between different iron oxide phases play a decisive role in determining electrocatalytic activity. The highest performance is observed for the coating containing a combination of hematite, magnetite, and maghemite phases, which exhibited the lowest overpotential of 349.7 mV at a current density of 10 $mA{\cdot}cm^{-2}$.

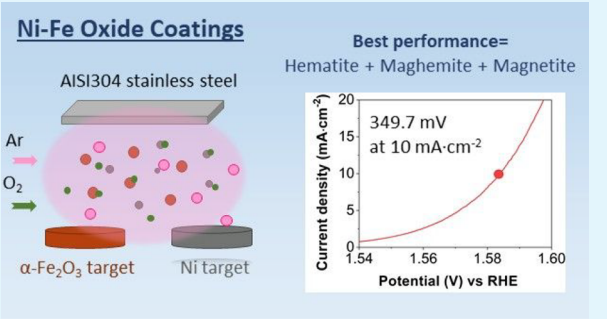

KEYWORDS: *oxygen evolution reaction, anion exchange membrane electrolysis, water splitting, iron oxides, magnetron sputtering*

1. INTRODUCTION

Aligning with the global goals of clean and sustainable energy,[1] the development of green hydrogen and green ammonia technologies is crucial. Despite their potential, current H_2 and NH_3 production methods rely heavily on fossil fuels, accounting for approximately 2% of global greenhouse gas emissions.[2] The shift to green hydrogen production via water electrolysis (WE) holds the potential to transform the global energy economy and accelerate the achievement of carbon neutrality. The two established WE technologies—alkaline (A-WE) and proton exchange membrane (PEM-WE) electrolysis—face economic challenges in achieving cost competitiveness with conventional H_2 production methods.[3] The anion exchange membrane (AEM-WE) electrolysis is an emerging technology that combines the low cost of A-WE and the high efficiency of PEM-WE. It utilizes abundant, inexpensive transition metals such as iron and their derivatives as catalysts, safe polymer membranes, and mildly alkaline electrolytes.[4] While scientific efforts are focused on the development of all critical components of AEM technology–namely catalysts, membranes, ionomers, membrane electrode assembly (MEA)[5]–a key challenge remains the advancement of efficient and stable electrocatalysts for both the hydrogen evolution reaction (HER) and the oxygen evolution reaction (OER). Transition metal oxides (TMO) and (oxy)hydroxides (TM-(O)OH) are considered as great candidates for this role due to their low overpotentials, long-term stability, fast kinetics, abundance and cost effectiveness.[6,7] Hematite (α-Fe_2O_3), which features a hexagonal crystal structure with Fe^{3+} ions occupying octahedral sites, is considered a promising material for OER due to its natural abundance, low toxicity, and environmental compatibility. Meanwhile, a spinel-type Fe_3O_4, can provide multiple oxidation states, high electrical conductivity, and favorable binding energies for OER intermediates.[8] However, Fe active sites often bind adsorbates too strongly. To address this, incorporating Ni—known for its tendency to bind intermediates too weakly—into Fe-based oxides may create a balanced system with varied oxidation states, improved conductivity, and more optimal adsorption characteristics for OER.[9] Although nickel–iron oxide systems have been extensively investigated worldwide, a comprehensive understanding of the optimal nickel content, suitable deposition techniques, and the impact of nickel incorporation on the phase structure of iron oxides remains limited. While porous morphologies are generally advantageous due to their increased active surface area, the vigorous evolution of oxygen during operation can lead to pore blockage,

Received: April 20, 2026
Revised: July 20, 2026
Accepted: July 23, 2026

ultimately resulting in a reduction of accessible surface area and catalytic performance.[10,11]

In this study, compact nickel-doped iron oxide thin films were synthesized by reactive magnetron sputtering (RMS), enabling precise control of film composition, microstructure, thickness, particle size, and crystallinity through systematic adjustment of deposition parameters. The present work aims to elucidate how Ni incorporation affects the formation and coexistence of different iron oxide polymorphs within the coatings. By tuning the deposition conditions, the relative contributions of hematite, magnetite, and maghemite phases were modulated, allowing the role of phase composition and interphase interactions in determining the electrocatalytic properties of the films to be systematically evaluated. This approach provides new insight into phase-driven optimization strategies for iron-oxide-based electrocatalysts.

2. MATERIALS AND METHODS

Nickel-doped iron oxide coatings were deposited on commercially available AISI304 type stainless steel plates with a geometric area of 1×3 cm^2 (Goodfellow, Germany) using the magnetron sputtering technique with Kurt J. Lesker PVD 75 system. Pure hematite (α-Fe_2O_3, 99.9% purity) and metallic nickel (99.99% purity) were used. Synthesis was performed in a 70/30% ratio of argon and oxygen gas. A direct current (DC) power source was used for the hematite target at 250 W and pulse direct current (PDC) was used for the nickel target at various power values (25–60 W). A base chamber pressure of 6.5×10^{-6} Torr was achieved and the operating pressure was fixed at levels between 1.3×10^{-2} and 1.8×10^{-2} Torr.

The crystal structure of the deposited coatings was investigated using a Bruker AXS D8 X-ray diffractometer. The operating conditions were as follows. Cu-K_α radiation with $\lambda = 1.54056 \times 10^{-10}$ m wavelength, Ni filter, anodic voltage 40 kV, position step of detector 0.02°, current strength 40 mA. Morphological peculiarities were analyzed with scanning electron microscopy (SEM) using Hitachi S-3400N equipment with Bruker Quad 5040 detector for energy dispersive X-ray spectroscopy (EDS). Raman analysis was conducted using a Renishaw inVia setup equipped with a 532 nm laser source, a 2400 L/mm grating and 100× objective. Surface topography was further investigated by high-resolution atomic force microscopy (AFM) using an instrument mounted in a vibration- and noise-isolated enclosure (Q-Box). XPS spectra were acquired in an Ultra High Vacuum (UHV) system with a base pressure of 2×10^{-10} mbar located at TEMA, University of Aveiro. The system is equipped with a hemispherical electron energy analyzer (SPECS Phoibos 150), a delay-line detector and a monochromatic AlKα (1486.74 eV) X-ray source. High resolution spectra were recorded at normal emission take-off angle and with a pass-energy of 20 eV, which provides an overall instrumental peak broadening of 0.5 eV.

Electrocatalytical evaluation was performed in 1.0 M KOH (Chempur, Poland) electrolyte in a three-electrode cell with nickel-doped iron oxide coatings on AISI304 as the working electrode, a platinum wire (geometric area 15 cm^2) as the counter electrode, and Ag,AgCl|$KCl_{(sat)}$ as the reference electrode. A potentiostat/galvanostat BioLogic SP-150 (BioLogic Science Instruments, Seyssinet-Pariset, France) with EC-Lab 10.39 software was used for recording and treating electrochemical data. Cyclic voltammetry (CV), chronoamperometry (CA), chronopotentiometry (CP) and potentiostatic electrochemical impedance spectroscopy (PEIS) were employed for the electrochemical characterization of the films. PEIS measurements were carried out with a sinus amplitude of 20 mV in the frequency range from 10^6 to 10^{-3} Hz at 1.544 V vs RHE. All potential values in this work are given according to the RHE with 85% iR compensation applied prior electrochemical measurements. The numerical fitting of PEIS results to the Randles circuit was performed using the Zview software from Scribner Associates. Constant phase elements (CPE, with impedance defined as $Z_{CPE} = [Y_0(i\omega)^n]^{-1}$, where Y_0 is a pseudo capacitance, n is a variable exponent $0 < n < 1$, and ω is the angular frequency) were used in place of capacitances[12] Then the CPE values were converted to effective capacitances using the Brug equation,[13,14] using Y_0, n and the values of the resistances in series (R_s) and parallel (R_{ct}) with respect to the CPE:

$$C = \sqrt[n]{Y_0}\left(\frac{1}{R_s} + \frac{1}{R_{ct}}\right)^{\frac{n-1}{n}} \quad (1)$$

The electrochemically active surface area (ECSA) was estimated from the double-layer capacitance (C_{dl}) obtained by CV rather than from EIS. The CV measurements were performed within a narrow non-Faradaic potential window (±20 mV the open-circuit potential), where the measured current is predominantly associated with double-layer charging. In contrast, the EIS measurements were conducted at the onset of the OER, where the electrode surface undergoes potential-dependent changes and the measured interfacial capacitance may include significant contributions from pseudocapacitance, surface-state charging, and adsorption of reaction intermediates. ECSA values were estimated from C_{dl}/C_s. Since no established C_s exists for dense Ni-doped iron oxide thin films, values reported for smooth metal electrodes (20–25 μF·cm^{-2}) and transition metal oxide electrodes (≈40 μF·cm^{-2}) were considered. In this work, C_s = 40 μF·cm^{-2} was used to facilitate comparison with the electrocatalysis literature.[15,16]

3. RESULTS AND DISCUSSION

3.1. Structural Analysis

To evaluate the doping efficiency and the correlation between dopant target power and its concentration in the deposited coatings, energy-dispersive X-ray spectroscopy (EDS) was employed. The results summarized in Table 1 indicate that the Ni content increases from 2.6 to 4.6 atom % as the target power is raised from 25 to 60 W. An increase in target power generally causes a linear or near-linear increase in dopant concentration during magnetron sputtering, particularly within a moderate power range.[17] However, the dependence of nickel concentration on target power is not linear. Deviations from a strict linear relationship may be related to the possible oxidation of the metallic nickel target surface in the Ar/O_2 atmosphere and the consequent formation of an insulating oxide layer.[18] The stability of this layer is governed by the competition between two processes: its removal by argon-ion bombardment and its regeneration by oxidation. At specific power levels, an imbalance between these processes leads to deviations in both the sputtering rate and the resulting film stoichiometry. This effect is particularly evident in the negligible change in Ni concentration observed when the Ni target power is increased from 40 to 50 W. However, because iron and nickel are among the elements present in the substrate, significant measurement errors are possible, so the results should be interpreted with caution. A slight increase in the iron concentration and decrease in the oxygen concentration was detected for the coating deposited at 60 W of Ni target power. Although EDS does not provide phase-specific information, this observation is consistent with the phase evolution identified by Raman spectroscopy, as discussed in the following section.

X-ray diffraction (XRD) was utilized to investigate the effect of nickel concentration on the crystallinity of the coatings and to examine the possible transformation of the initial hematite

https://doi.org/10.1021/acsaem.6c01330
ACS Appl. Energy Mater. XXXX, XXX, XXX–XXX

Table 1. Elemental Composition and Crystallinity Percentage of Iron-Nickel Oxide Coatings on AISI304 Stainless Steel

parameter		nickel target power (W) 25	30	40	50	60
elemental concentration (atom %)	Fe	49.3 ± 0.8	49.4 ± 0.7	49.0 ± 0.4	49.5 ± 2.0	54.2 ± 0.6
	Ni	2.6 ± 0.1	2.8 ± 0.2	3.1 ± 0.1	3.2 ± 0.1	4.6 ± 0.2
	O	37.1 ± 1.0	37.6 ± 0.6	35.7 ± 0.2	34.6 ± 1.0	25.2 ± 1.5
	balance	up to 100%				
crystallinity percentage (%)		67.1	35.4	16.2	31.0	32.1

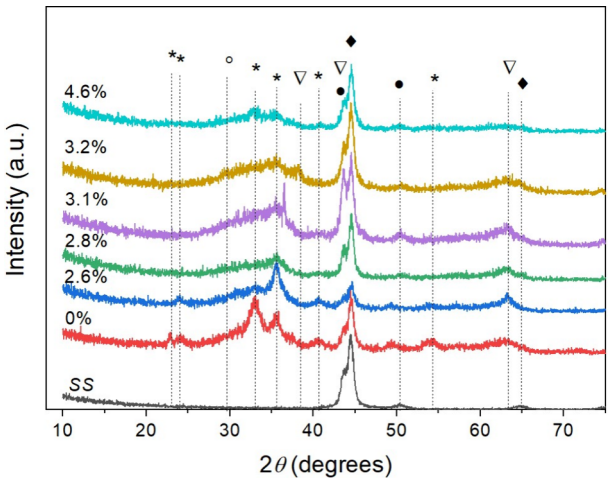

Figure 1. XRD patterns of uncoated AISI304 substrate (SS), undoped iron oxide and nickel-doped iron oxide coatings with different Ni concentrations. Symbols: *—Fe_2O_3 (ICDD PDF No. 33–0664), ○—Fe_3O_4 (ICDD PDF No. 19–629), ▽—NiO (ICDD PDF No. 73–1523), ●—Ni-Cr-Fe (ICDD PDF No. 33–397), ◆—Fe-Cr (ICDD PDF No. 34–396).

crystalline phase into other iron oxide phases. As evidenced by the results presented in Figure 1, the incorporation of nickel into the synthesis procedure exerts a pronounced influence on the crystallinity of the doped coatings in comparison with the undoped coating prepared under identical conditions. Although the α-Fe_2O_3 phase (ICDD PDF No. 33–0664) with the (012), (104), (113), (024), and (116) reflections positioned at 2θ = 23.94°, 32.88°, 40.72°, 50.00°, and 53.84°, respectively, dominates the structure of the coatings, traces characteristic of the Fe_3O_4 phase (ICDD PDF No. 19–629) were also observed. Due to the amorphous nature of the coatings, the determination of the phases of nickel oxide compounds becomes hampered, as the peaks of some possible compounds, e.g., $NiFe_2O_4$, overlap with the peaks of α-Fe_2O_3 in the pattern, especially the most intense peak at 2θ = 35.6°. However, low intensity peaks characteristic of nickel oxide (NiO, ICDD PDF No. 73–1523) at 2θ = 37.21° and 43.15° are detected in the coating diffractogram.

The crystallinity of the coatings was also quantitatively assessed based on XRD results. The calculations of crystallinity percentage (CP) (Table 1) reveal that a slight increase in nickel concentration from 2.6 to 2.8% leads to an almost twofold reduction in crystallinity, decreasing from 67.1 to 35.4%. This behavior may be attributed to the incorporation of nickel ions into the iron oxide lattice during reactive magnetron sputtering, which likely promotes the formation of lattice defects, such as oxygen vacancies, thereby favoring the development of an amorphous structure. A further increase in nickel concentration to 3.1% resulted in an additional decrease in the CP to 16.2%, indicating substantial phase rearrangement during the sputtering process. Upon increasing the Ni target power from 40 to 50 W, as discussed previously, the change in nickel concentration determined by EDS analysis was negligible. However, crystallinity percentage calculations showed that the coating with 3.2% nickel exhibited a markedly higher crystalline fraction than the coating with 3.1% nickel. These findings support the hypothesis that, within the 40–50 W power range, a competitive interplay exists between the formation and degradation of the target passivation layer, which may create conditions conducive to the formation of amorphous coatings. A further increase in nickel concentration to 4.6% does not result in a significant change in crystallinity relative to the coating containing 3.2% Ni, with the crystalline fraction remaining at approximately 32.1%. This behavior can be attributed to operation at target powers exceeding the regime dominated by target passivation, under which oxide film formation becomes stabilized and sputtering proceeds without pronounced fluctuations. In this regime, the sputtering rate increases with target power, leading to a more constant flux of sputtered species and a steadier growth environment, which suppresses large variations in phase composition and crystallinity.

Raman analysis of nickel-doped iron oxide coatings revealed more scattered results among coatings with different Ni concentrations (Figure 2). The undoped iron oxide coating deposited under the same conditions presented a combination of several phases of iron oxide (Figure S1). α-Fe_2O_3 structure was confirmed with symmetric stretching E_g vibrations at 292, 411, and 613 cm^{-1} and antisymmetric bonding peak (A_{1g}) at 221 cm^{-1}.[19] The presence of a maghemite (γ-Fe_2O_3) was suggested by the low-intensity E_g vibrations at 507 cm^{-1} and A_{1g} peak at 688 cm^{-1}. Only the most intense A_{1g} peak of a spinel-type magnetite (Fe_3O_4) was recorded at 668 cm^{-1} assuming that Fe(III) is the dominant oxidation state in the deposited undoped iron oxide coatings.

The incorporation of nickel into the structure during synthesis at the lowest concentration of 2.6 atom % adjusts the iron oxide structure while maintaining the oxidation state of Fe^{3+} in the compounds as prevailing. However, apart from the peaks of hematite and maghemite, all four peaks characteristic of magnetite were prominent in the spectrum, including two T_{2g} peaks at 193 and 538 cm^{-1}, E_g peak at 306 cm^{-1} and the most intensive A_{1g} peak at 668 cm^{-1}. This observation may imply a more pronounced reduction of iron(III) within the deposition chamber during the reactive magnetron sputtering process, likely facilitated by the concurrent oxidation of metallic nickel particles into their respective oxide phases. Partial substitution of Fe ions with Ni ions in the spinel structure of Fe_3O_4 is supported by the presence of T_{2g} asymmetric Fe-O or Ni-O bonding vibrations at 570 cm^{-1} and A_{1g} symmetric stretching Fe-O vibrations at 691 cm^{-1} characteristic to $NiFe_2O_4$.[20] Quantitative Raman peak deconvolution (Table S1) confirms

https://doi.org/10.1021/acsaem.6c01330
ACS Appl. Energy Mater. XXXX, XXX, XXX–XXX

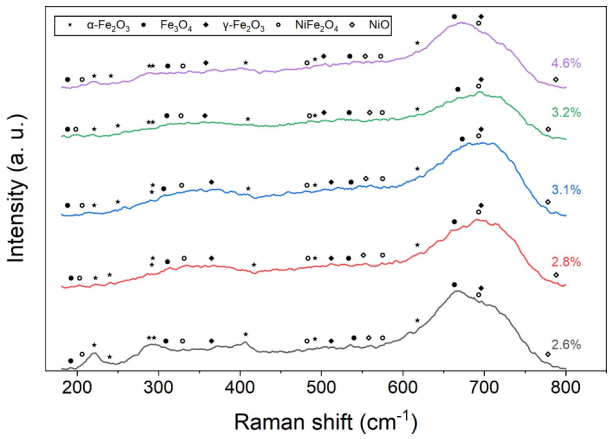

Figure 2. Raman spectra of iron-nickel oxide coatings with different Ni concentrations.

that γ-Fe_2O_3 is the dominant phase (53.5%), followed by α-Fe_2O_3 (23.7%), $NiFe_2O_4$ (15.7%), and smaller contributions from Fe_3O_4 (6.4%) and NiO (0.7%).

Further increment in Ni concentration to 2.8 atom % is favorable for the formation of inverse spinel-type maghemite phase in which some of the Fe^{3+} ions occupy tetrahedral positions surrounded by four instead of six O^{2-} ions, thus creating cation vacancies.[21] Although the most characteristic hematite bands at 292 and 412 cm^{-1} become considerably less pronounced in the experimental spectrum, Raman fitting indicates that α-Fe_2O_3 still contributes approximately 24.8% of the overall spectral response. While the most characteristic magnetite peaks at 306 and 668 cm^{-1} are present in the spectrum, a noticeable shift of the broadened peak within the 650–750 cm^{-1} range is observed. This shift can be attributed to several factors. Firstly, while both maghemite and magnetite share a spinel crystal structure with Fe(III) ions occupying tetrahedral sites—contributing to this spectral feature—the observed shift toward the maghemite region may indicate the predominance of maghemite in the coating. Additionally, the partial substitution of iron ions with nickel ions in the nickel ferrite lattice likely contributes to both the peak broadening and its spectral shift.[20] This interpretation is supported by the deconvolution results, which identify γ-Fe_2O_3 as the major component (50.9%) together with an increased $NiFe_2O_4$ fraction (17.9%). Secondly, XRD analysis suggests a significant drop in the coating crystallinity (35.4% compared to 67.1% for 2.6% Ni concentration), which is associated with randomly oriented dangling bonds.[22] This structural disorder typically results in broader, less intense Raman peaks. A similar evolution is observed for the coating containing 3.1 atom % Ni. Although characteristic $NiFe_2O_4$ band near 560 cm^{-1} is not clearly resolved in the spectrum due to the peak overlap and band broadening, Raman fitting reveals that nickel ferrite accounts for 23.8% of the fitted spectrum, representing the highest concentration among all investigated samples. Simultaneously, the γ-Fe_2O_3 contribution decreases to 44.0% while Fe_3O_4 remain relatively constant (5.2%) and NiO contributes only 1.0%. These results indicate enhanced incorporation of Ni into the spinel lattice rather than extensive segregation into NiO, despite the visual dominance of magnetite-related features.

The Raman spectrum of the iron oxide coating doped with 3.2% of Ni reveals the presence of distinct peaks corresponding to hematite, maghemite, magnetite, and nickel ferrite, indicating the coexistence of multiple iron oxide phases. Quantitative fitting identifies γ-Fe_2O_3 as the predominant phase (47.8%), followed by α-Fe_2O_3 (29.7%), $NiFe_2O_4$ (16.4%), Fe_3O_4 (5.4%), and a minor NiO contribution (0.7%), confirming that the multiphase character of the coating is retained despite increasing nickel incorporation. Although the Ni concentration determined by EDS (Table 1) is slightly higher than that of the 3.1 atom % Ni coating, the fitted $NiFe_2O_4$ fraction decreases from 23.8 to 16.4%. As mentioned previously, the difference in Ni concentration between these coatings (0.1 atom %) is close to the uncertainty associated with EDS quantification, especially due to the presence of nickel in the substrate. Therefore, the measured Ni concentrations are regarded as approximate. Nevertheless, the reduction of $NiFe_2O_4$ fraction supports the assumption of partial target passivation during reactive magnetron sputtering in the power range of 40–50 W. Formation of an oxide layer on the nickel target surface can reduce the sputtering yield of metallic Ni, thereby decreasing the flux of nickel atoms reaching the substrate and limiting $NiFe_2O_4$ formation. Consequently, a larger fraction of iron remains incorporated in hematite and maghemite phases, as reflected by the increased α-Fe_2O_3 contribution.

At the highest Ni concentration of 4.6 atom %, the broad and nearly symmetrical band around 670 cm^{-1} suggests a stronger contribution from spinel-type phases. Although the experimental spectrum does not display clearly distinguishable maghemite bands because of extensive spectral overlap, Raman peak fitting reveals that γ-Fe_2O_3 remains the largest phase fraction (39.5%), accompanied by increased contributions from $NiFe_2O_4$ (20.0%) and Fe_3O_4 (9.4%), while α-Fe_2O_3 accounts for 30.2% of the fitted spectrum. The increase in the magnetite and nickel ferrite fractions indicates that higher Ni concentrations favor the stabilization of spinel-type oxide phases, whereas the consistently low NiO content (<1%) suggests that most nickel is incorporated into the ferrite lattice rather than forming a separate nickel oxide phase. The Raman analysis of the coating with 4.6 atom % Ni provided further insight into the compositional changes previously observed by EDS (Table 1). As discussed in the EDS results, the coating deposited at the highest Ni target power exhibited a slight increase in iron concentration followed by the decrease in oxygen concentration. The Raman peak deconvolution revealed that this trend could be related to the increase in the Fe_3O_4 phase fraction that possesses the lower O/Fe atomic ratio (4/3) compared to the γ-Fe_2O_3 phase (3/2) which fraction reduced during synthesis.

Scanning electron microscopy (SEM) analysis was performed on as-deposited coatings without an additional gold layer (Figures 3 and S2). Examination of the micrographs indicates that the nickel target power applied during synthesis significantly influences the resulting coating morphology. All coatings are compact and closely replicate the underlying stainless steel surface morphology, indicating good conformity and coverage. In general, higher power increases the sputtering rate and particle flux, which raises the probability of particle–particle interactions both in the plasma phase and upon arrival at the substrate, thereby favoring agglomeration and cluster formation.[23] Analysis of particle size as a function of nickel target power (and corresponding nickel concentration) shows that at the lowest power (25 W), particles are uniformly distributed with diameters ranging from 20 to 70 nm. At 30 W, particles of 30–70 nm remain predominant; however, isolated clusters

https://doi.org/10.1021/acsaem.6c01330
ACS Appl. Energy Mater. XXXX, XXX, XXX–XXX

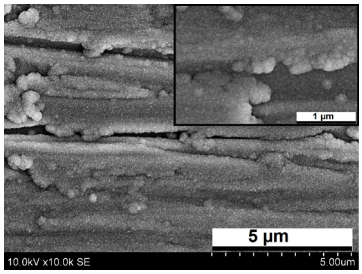

Figure 3. SEM micrographs of nickel-doped iron oxide, with the inset depicting the nanocluster (20–50 nm) microstructure.

with diameters of 150–250 nm begin to appear. Further increases in power to 40 and 50 W promote the formation of denser regions enriched with larger particles, rather than discrete clusters, although the dominant particle size remains below 80 nm. The increasing kinetic energy of sputtered species enhances surface diffusion, promoting coalescence into larger features and the development of particle-rich zones. At a target power of 60 W, the coating exhibits more homogeneous growth compared to the previously analyzed samples, with a relatively balanced distribution of smaller particles (35–50 nm) and larger particles (70–100 nm). It may arise from a dynamic balance between increased nucleation density and enhanced surface mobility, resulting in simultaneous formation of new nuclei and controlled growth of existing particles.

The cross-sectional SEM images (Figure S3) revealed that the film thickness increased slightly from 373 to 391 nm as the Ni target power was increased from 25 to 30 W. This increase can be attributed to the higher sputtering yield of the Ni target, which results in a higher deposition rate. However, further increasing the Ni target power caused the film thickness to decrease progressively, reaching 260 nm at 60 W. At higher target powers, energetic ion bombardment during reactive magnetron sputtering becomes more significant, enhancing the re-sputtering of weakly bonded surface atoms and thereby reducing the net deposition rate. Simultaneously, increased Ni incorporation promotes grain refinement and enhanced atomic packing, resulting in the formation of thinner but denser films.

Surface roughness of all synthesized samples was evaluated by AFM (Table S2). The results revealed that the surface roughness varied with the applied Ni target power, initially increasing and then decreasing at higher powers. This behavior can be attributed to the competing effects of Ni incorporation on thin-film nucleation and crystal growth during reactive magnetron sputtering. At low Ni target powers (25 and 30 W), the films exhibited relatively smooth surfaces when measured S_q values for 10 × 10 µm areas did not exceed 25 nm. The relatively smooth surface is obtained due to uniform grain growth and sufficient adatom mobility, allowing deposited species to diffuse to energetically favorable sites.[24] As the Ni target power increased up to 40 W, greater Ni incorporation introduced lattice distortion and promoted the formation of additional nucleation sites, resulting in grain competition, non-uniform crystal growth, and more pronounced surface features. Simultaneously, the higher deposition rate reduced adatom surface diffusion and enhanced shadowing effects, contributing to an increase in surface roughness up to 50 nm. With further increasing Ni target power to 50 and 60 W, the roughness decreased to 40 and 20 nm, respectively, indicating a transition in the dominant growth mechanism. At higher Ni concentrations, grain growth was likely to be inhibited by grain-boundary pinning and continuous renucleation, leading to grain refinement and the formation of a denser, more homogeneous microstructure.

XPS was employed to investigate the surface chemical composition and oxidation states of the synthesized coatings (Table S3). The Fe 2p spectra of all coatings exhibit the characteristic spin-orbit doublet (Fe 2p3/2 and Fe 2p1/2, separated by ≈13.6 eV) together with the shake-up satellite structure and multiplet splitting that are diagnostic of high-spin Fe oxide environments and that make the Fe 2p envelope inherently more complex to deconvolute than a simple two-peak model.[25,26] In the present coatings, curve fitting resolved Fe^{2+} and Fe^{3+} contributions within the Fe 2p3/2 multiplet, and the resulting fractions were cross-checked against the Fe-associated component of the O1s line shape, which independently reports on the local Fe-O coordination through its lattice-oxygen sub-components (Table S3). Across the as-deposited series, the two channels agree within 1.5–2 percentage points at every composition (e.g., 61.98/38.02% from Fe 2p versus 60.36/37.03% from O 1s at 25 W), which supports the internal consistency of the peak assignment rather than indicating two chemically distinct Fe populations. All as-deposited coatings display a mixed-valence Fe^{2+}/Fe^{3+} surface, with Fe^{2+} fractions between 58 and 63%, i.e., a surface substantially richer in Fe^{2+} than pure hematite (exclusively Fe^{3+}) but broadly compatible with the Fe^{2+}–Fe^{3+} stoichiometry expected for magnetite-type (Fe_3O_4) and some part of nickel-ferrite-type ($NiFe_2O_4$) spinel environments, which is consistent with the multiphase hematite/magnetite/maghemite/nickel-ferrite assemblage already identified by Raman deconvolution (Table S1) and by XRD (Figure 1). The film deposited at 50 W (3.2 atom % Ni) is the only composition for which the surface Fe^{3+} fraction exceeds Fe^{2+} by more than a marginal amount (41.88 versus 58.12% from Fe 2p), indicating a comparatively more oxidized, hematite/maghemite-like near-surface layer. Because this coating also delivers the lowest overpotential at 100 mA·cm^{-2} and the smallest Tafel slope among all samples (Table 2), the XPS result reinforces the argument that the electrocatalytic response is governed by the specific balance of iron oxide phases and their associated Fe oxidation states rather than by nickel content alone; an Fe^{3+}-enriched, defect-tolerant surface appears here to combine favorably with the electronic conductivity retained from the coexisting Fe_3O_4 and some part of the fraction of nickel ferrite.

The Ni 2p spectra were deconvoluted into Ni^{2+} and Ni^{3+} contributions superimposed on the characteristic Ni 2p shake-up satellite envelope, which is required for reliable quantification of mixed Ni oxidation states in $NiO/NiFe_2O_4/NiOOH$-type systems.[25] At every composition, the sum of the surface Ni^{2+} and Ni^{3+} fractions is small relative to Fe (2.6–5.0 atom %), consistent with Ni acting as a dilute substitutional dopant within the iron oxide lattice rather than forming an appreciable separate NiO phase, in line with the low (<1%) NiO content extracted from Raman deconvolution across the whole series (Table S1). A composition-dependent trend in Ni speciation is nevertheless apparent: at low-to-intermediate Ni loading (25–50 W, 2.6–3.2 atom % Ni), the surface Ni is predominantly Ni^{3+} (e.g., 0.09% Ni^{2+} versus 3.16% Ni^{3+} at 40 W), whereas at the highest loading (60 W, 4.6 atom % Ni) this ratio inverts, with Ni^{2+} (3.11%) exceeding Ni^{3+} (1.86%). Dilute, isolated

https://doi.org/10.1021/acsaem.6c01330
ACS Appl. Energy Mater. XXXX, XXX, XXX–XXX

Table 2. Electrocatalytical Parameters of Nickel-Doped Iron Oxide Coatings in 1.0 M KOH[a]

Ni concentration (atom %)	η (±0.1 mV) at 10 mA·cm^{-2}	η (±0.1 mV) at 100 mA·cm^{-2}	b (±1 mV·dec^{-1})	
0	355.8	448.5	23	45
2.6	352.2	411.7	32	39
2.8	357.2	453.0	31	41
3.1	360.3	464.8	31	39
3.2	354.0	410.2	28	34
4.6	349.7	431.9	32	45

[a]Tafel slopes are given for a (left) high and a low (right) potential range.

Ni substituting for Fe^{3+} within the hematite/maghemite/nickel ferrite framework is charge-compensated most readily as Ni^{3+}, whereas at higher Ni loading a larger fraction of Ni is accommodated within a stoichiometric $NiFe_2O_4$ spinel environment, in which Ni conventionally occupies octahedral sites as Ni^{2+}. This is consistent with the Raman-derived $NiFe_2O_4$ fraction increasing monotonically from 15.7 to 20.0% between the lowest and highest Ni-target-power coatings (Table S1).

The O 1s spectra of all coatings were resolved into a main lattice-oxygen component (metal-O^2, the dominant contribution in every sample) together with higher-binding-energy components generally assigned in the literature to hydroxyl groups, defect-associated oxygen and adsorbed molecular water. Because the strict correspondence between the 531–532 eV O 1s feature and true oxygen vacancies has been repeatedly and explicitly challenged a vacant lattice site cannot itself emit a photoelectron, and the same binding-energy region is populated by surface hydroxyls, adsorbed water and defect-related metal-oxygen environments that are spectroscopically indistinguishable from vacancies by O1s alone.[27−29] The higher-binding-energy O1s components reported here are interpreted conservatively as a hydroxylated/defective near-surface oxide rather than as a direct, quantitative measure of the oxygen-vacancy concentration. Within this conservative framework, the relative intensity of the non-lattice O1s components tracks the same compositional trend already identified by XRD, i.e., coatings with lower crystallinity percentage (Table 1) display a proportionally larger hydroxylated/defective oxygen contribution, consistent with the greater density of dangling bonds and undercoordinated surface cations expected for amorphous, Ni-perturbed iron oxide networks.[22] This defective, hydroxylated character is mechanistically favorable for OER, since surface hydroxyl groups and undercoordinated metal-oxygen sites are widely regarded as precursors for, or direct participants in, the adsorption of OH- intermediates during the first electron-transfer step of the reaction.

Quantitative comparison of the XPS-derived atomic concentrations with the bulk EDS values (Table 1) provides additional insight into the near-surface distribution of Ni. Summing the Ni^{2+} and Ni^{3+} fractions gives a total surface Ni content of 2.6, 3.0, 3.3, 3.9 and 5.0 atom % for the films deposited at 25, 30, 40, 50 and 60 W, respectively, which are numerically close to, and for the two highest-power films slightly higher than, the corresponding EDS-derived bulk values of 2.6, 2.8, 3.1, 3.2 and 4.6 atom %. This small but systematic surface excess at 50 and 60 W (+0.7 and + 0.4 atom % relative to EDS, respectively) is compatible with mild surface segregation of Ni toward the outermost 5–10 nm probed by XPS, an effect that a bulk-averaging technique such as EDS is not able to resolve. The formation of a mixed Fe^{2+}/Fe^{3+} surface in every as-deposited coating, rather than a purely Fe^{3+} hematite-like surface, is a direct consequence of the reactive magnetron sputtering conditions employed. Reactive sputtering of an oxide target in an Ar/O_2 mixture is intrinsically sensitive to the instantaneous oxidation state of the target surface, which is itself governed by a dynamic competition between argon-ion-induced target erosion (which exposes reduced, sub-stoichiometric metal) and re-oxidation by the reactive gas.[18] Because the deposition rate, the flux of oxidized versus metallic species reaching the growing film, and the resulting film stoichiometry are all coupled to this target-surface equilibrium, a degree of oxygen sub-stoichiometry and hence a fraction of reduced Fe^{2+} cations is essentially unavoidable in RMS-grown iron oxide films, even when the nominal target material (α-Fe_2O_3) contains only Fe^{3+}.

3.2. Electrocatalytic Activity in Oxygen Evolution

The electrocatalytic properties of nickel-doped iron oxide coatings were evaluated using various electrochemical techniques. The LSV curves illustrate how the current density of the coatings responds to changes in potential within the anodic region (Figure 4A). These results indicate that the activity for oxygen evolution does not directly correlate with the nickel concentration. Instead, factors such as the distribution of iron oxide phases, along with the degree of crystallinity, appear to have a significantly greater impact on electrocatalytic performance.

XRD analysis (Figure 1) of the doped coatings revealed that, compared to the undoped iron oxide coating, the incorporation of nickel promotes the formation of an amorphous structure. The resulting long-range disorder can lead to unsaturated coordination sites and structural defects, which are considered as advantageous for electrocatalysis. However, this disorder may also contribute to reduced electrical conductivity.[22] Therefore, phase engineering emerges as an effective strategy to develop electrocatalytically active materials by leveraging the high density of active sites inherent to amorphous phases, while maintaining the stability and adequate conductivity associated with crystalline structures. Raman spectroscopy indicated the conversion between different iron oxide crystal phases while altering the power of the nickel target, which can facilitate the generation of disordered domains and, consequently, enhance the concentration of active sites. During LSV measurements the coating containing 2.6 atom % Ni exhibited one of the lowest overpotentials at both 10 and 100 mA·cm^{-2} (Table 2). According to the Raman analysis, this sample was dominated by the γ-Fe_2O_3 phase, which is generally reported to possess higher electronic conductivity and a greater density of surface defects than α-Fe_2O_3. These characteristics likely facilitate electron transport and provide a larger number of catalytically active sites, contributing to the enhanced OER performance. Increasing the Ni concentration to 2.8 atom % resulted in

https://doi.org/10.1021/acsaem.6c01330
ACS Appl. Energy Mater. XXXX, XXX, XXX−XXX

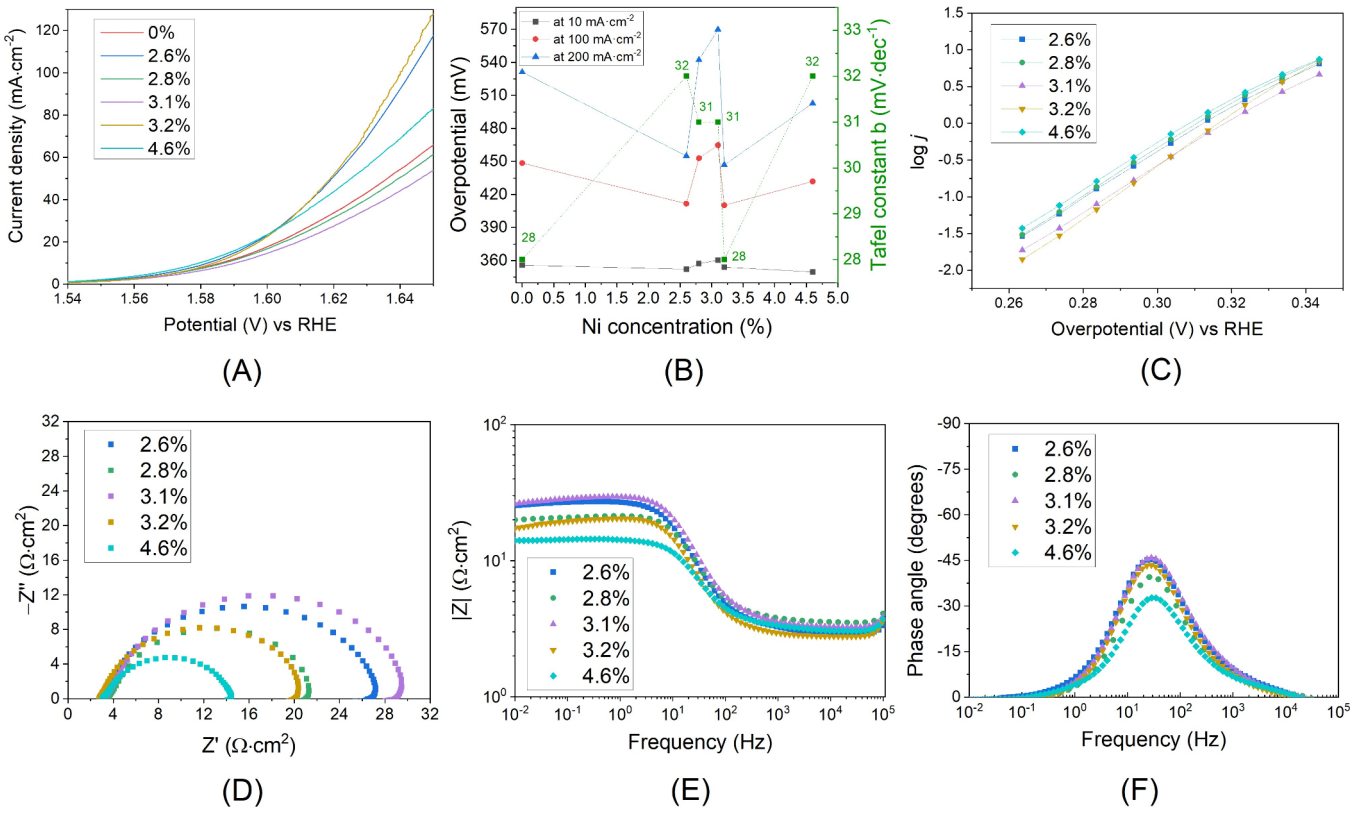

Figure 4. Linear sweep voltammograms (A), overpotential at various current densities (B), Tafel (C), Nyquist (D) and Bode (E, F) plots of nickel-doped iron oxide coatings in 1.0 M KOH at 20 mV·s.$^{-1}$

higher overpotentials, particularly at 100 mA·cm^{-2}. Although the $NiFe_2O_4$ content increased, the fraction of γ-Fe_2O_3 decreased slightly (from 53.5 to 50.9%), suggesting that the increased spinel content did not fully compensate for the reduction in the conductive and defect-rich maghemite phase. A further increase in the Ni concentration to 3.1 atom % led to an additional decline in OER activity despite the highest $NiFe_2O_4$ fraction (23.8%). This coating also contained one of the lowest γ-Fe_2O_3 contents (44.0%) and exhibited the highest surface roughness among all samples. While a rougher surface generally provides a larger electrochemically accessible area, excessive roughness may become detrimental during the oxygen evolution reaction. The pronounced surface features can promote bubble retention within surface valleys, partially blocking active sites and hindering electrolyte access, particularly at higher current densities where oxygen evolution is more vigorous.

Further increasing the Ni concentration to 3.2 atom % significantly improved the OER performance, yielding the lowest overpotential at 100 mA·cm^{-2} and the smallest Tafel slope. Although the phase composition did not differ substantially from that of the neighboring compositions, this coating exhibited a more balanced combination of α-Fe_2O_3, γ-Fe_2O_3, Fe_3O_4, and $NiFe_2O_4$ together with moderate surface roughness (<40 nm). This combination likely provided an optimal compromise between electrical conductivity, the density of catalytically active sites, and efficient mass transport, making this coating the most effective electrocatalyst among those investigated. The coating containing 4.6 atom % Ni exhibited the lowest overpotential at 10 mA·cm^{-2}; however, its performance deteriorated at 100 mA·cm^{-2}. This behavior may be associated with the further decrease in the γ-Fe_2O_3 fraction to 39.5% and the lowest surface roughness among all samples. Although the increased Fe_3O_4 content may enhance electronic conductivity, the reduced amount of the defect-rich maghemite phase together with the smoother surface is likely to decrease the density and accessibility of active sites, thereby limiting the catalytic performance under high-current operating conditions. Overall, these results demonstrate that maximizing the concentration of an individual phase, such as $NiFe_2O_4$, is insufficient to optimize the OER activity. Instead, the best performance is achieved through a balanced phase composition combined with favorable surface morphology. Although the difference in activity between coatings with 2.6 and 3.2% of Ni appears modest, as they both require only 56–60 mV to increase the current density from 10 to 100 mA·cm^{-2}, staircase chronopotentiometry measurements (Figure S5) reveal that higher nickel content in the iron oxide coatings offers a distinct advantage—likely due to an increased density of active sites and structural defects. At industrially relevant current densities, the coating with 3.2% of Ni demonstrates more efficient oxygen evolution, as evidenced by a lower overpotential compared to the lower-nickel sample.

Normalization of the OER activity to the ECSA (Table S4) did not substantially change the overall performance trend obtained using the geometric electrode area (Figure S6). The ranking of the coatings remained essentially unchanged, indicating that the differences in electrocatalytic activity cannot be attributed solely to variations in the electrochemically active surface area. Notably, ECSA normalization more clearly

https://doi.org/10.1021/acsaem.6c01330
ACS Appl. Energy Mater. XXXX, XXX, XXX–XXX

highlighted the superior activity of the coating containing 2.6 atom % Ni relative to the coating with 3.1 atom % Ni. These results suggest that the observed differences in OER performance are primarily governed by the combined effects of phase composition and microstructural characteristics, while the contribution of the electrochemically active surface area is comparatively less significant.

In evaluating the efficiency of coatings for catalyzing oxygen evolution and their possible application at industrial level, identifying the rate-determining step is particularly critical. Despite occurring under alkaline conditions, oxygen evolution remains kinetically unfavorable, as the formation of one O_2 molecule from hydroxide ions requires the removal of four electrons. The Tafel slope (b), derived from the Tafel equation describing the relationship between current density and overpotential, provides insight into which step of the hydroxide ion oxidation process is most kinetically hindered. A lower Tafel slope generally indicates that the rate-limiting step is at the end of the four-electron process, and is therefore characteristic of a more efficient catalyst. Tafel plots (Figure 4C) were derived from potential-controlled electrolysis data (Figure S4) in the range of 1.49–1.57 V, with the corresponding Tafel slopes (b values) summarized in Table 2. This potential window was selected based on previously recorded LSV curves (Figure 4A) to emphasize the onset region of the oxygen evolution. The Tafel plots display a noticeable inflection in the middle of the analyzed region, indicating a change in the rate-determining step between the onset and higher current densities. Based on previous simulations aimed to establish the relationship between Tafel slopes and the anodic transfer coefficient (or symmetry coefficient for a complex electron reactions),[30] Tafel slopes in the range of 28–32 mV can be subject to ambiguous interpretation. The simulations indicated that such values at low overpotentials may correspond either to the removal of the third electron during the oxidation of M–O to M–OOH, or to an earlier step involving the release of the second electron during the transition from M–OH to M–O.[4] Meanwhile, a further increase in overpotential clearly suggests that the rate-determining step shifts earlier in the reaction pathway, with the release of the second electron becoming the key factor governing the overall reaction kinetics.

3.3. Corrosion Behavior

According to the ionization tendency, metallic components in the oxide state are more thermodynamically stable than in their metallic form in aqueous solutions.[31] However, electrochemical redox reactions that inevitably occur at the surface of the active material can ultimately accelerate catalyst surface degradation and reduce catalytic activity. Therefore, corrosion monitoring and quantitative evaluation of its parameters enables the prediction of surface durability, which is critical for assessing their suitability in industrial applications. A well-known technique of Tafel extrapolation was employed to determine the general corrosion.[32] The results presented in Figure S7 and Table 3 reveal the intensity of both anodic and cathodic processes occurring on the surface of the coatings in an alkaline medium. The anodic process in metallic materials involves the oxidation of metal ions to higher oxidation states, while the cathodic process corresponds to the diffusion of dissolved oxygen to the interface, where it undergoes reduction to form OH^-. Tafel extrapolation results indicated that the corrosion potential values for the various nickel-doped iron oxide coatings exhibit some variations, but all fall within the range of 900–1000 mV vs RHE. No clear correlation was observed between the nickel concentration in the coatings and their E_{corr}. In contrast, the corrosion current values demonstrate a more systematic trend. Linear polarization measurements revealed that coatings with lower nickel concentration of 2.6 and 2.8 atom % exhibit significantly higher j_{corr}—at least twice those of coatings with higher Ni concentrations – indicating a greater propensity for surface redox reactions. The relative contributions of cathodic and anodic processes to long-term surface changes were inferred from the Tafel slopes of the cathodic and anodic branches—β_c and β_a, respectively. The values of these slopes suggest that cathodic processes, related to O_2 reduction, predominate across all coatings, as they are characterized by lower overpotentials for a decade of current density. Comparison of the β_a values indicates that increasing the nickel concentration promotes greater involvement of the doped coatings in oxidation processes. A correlation was also observed between the crystallinity of the active material and the β_a value. XRD analysis revealed that higher nickel concentrations lead to increased amorphousness of the coatings, suggesting that the lack of a well-defined crystalline structure may enhance redox activity, not only at the surface but potentially within the bulk of the catalyst as well. In contrast to the behavior observed in anodic reactions, there is an inverse relationship between β_c—which indicates the intensity of the cathodic reaction – and the degree of amorphousness in the coatings. Coatings with a predominantly amorphous structure exhibit higher overpotentials, suggesting that the reduction of oxygen molecules, whether adsorbed on the surface or intercalated into deeper layers, proceeds more slowly. This behavior may be attributed to the long-range structural disorder introduced during coating formation, which likely promotes the development of configurations more tolerant to oxygen deficiency. In comparison, more crystalline coatings tend to incorporate oxygen molecules into their structure more readily, effectively filling existing vacancies.

3.4. Electrochemical Impedance Measurements

Electrochemical impedance spectroscopy was employed to investigate the electrode–electrolyte interface and to gain insight into the mechanism and kinetics of the OER. The measurements were performed at a pre-oxygen evolution potential of 1.544 V in order to accurately determine the charge-transfer resistance but to avoid noise caused by intensive oxygen

Table 3. Corrosion Parameters of Nickel-Doped Iron Oxide Coatings in 1.0 M KOH

Ni concentration (%)	E_{corr} (±0.1 mV)	j_{corr} (±0.001 μA·cm^{-2})	β_a (±0.1 mV)	β_c (±0.1 mV)	corrosion rate (±0.001 μm per year)
2.6	970.7	0.033	98.6	10.1	0.367
2.8	902.3	0.029	128.8	11.3	0.353
3.1	991.9	0.008	51.9	18.6	0.091
3.2	894.1	0.003	32.1	22.4	0.033
4.6	974.2	0.014	77.5	12.4	0.159

https://doi.org/10.1021/acsaem.6c01330
ACS Appl. Energy Mater. XXXX, XXX, XXX–XXX

Table 4. Quantitative Parameters of EIS Fittings According to the Following Equivalent Circuit: $R_s + C_{dl}/R_{ct}$

Ni concentration (%)	R_s (±0.01 Ω·cm^{-2})	$Y_{0,dl}$ (±0.01 mF·s^{n-1}·cm^{-2})	n_{dl} (±0.001)	C_{dl} (±0.001 mF·cm^{-2})	R_{ct} (±0.01 Ω·cm^{-2})	X^2
2.6	3.22	1.17	0.885	0.558	24.72	6.1×10^{-4}
2.8	3.71	1.15	0.890	0.572	18.42	5.9×10^{-4}
3.1	3.40	1.01	0.877	0.449	27.47	7.0×10^{-4}
3.2	2.90	1.30	0.899	0.685	18.35	5.1×10^{-4}
4.6	3.22	1.86	0.851	0.727	11.46	1.6×10^{-4}

bubble formation at higher potentials. The obtained results are presented as Nyquist (Figure 4D) and Bode (Figure 4E,F) plots. For all investigated samples, the impedance spectra exhibit characteristic semicircles corresponding to a single time constant. However, their distribution does not follow a systematic trend with respect to Ni concentration. The experimental data were fitted using an equivalent circuit model $R_s + C_{dl}/R_{ct}$, consisting of the series resistance (R_s), double-layer capacitance (C_{dl}), and charge-transfer resistance (R_{ct}). The extracted values of the circuit elements are summarized in Table 4. Although magnetron sputtering typically produces compact coatings with low surface roughness (Figures 3, S2, and S3; Table S2), the relatively high double-layer capacitance values suggest that the coating surfaces may possess nanoscale structural features accompanied by porous hydration layers of oxyhydroxides. Furthermore, nickel is known to undergo the reversible redox transition $Ni^{(II)}/Ni^{(III)}$, which introduces pseudocapacitive behavior and contributes to the increase in the apparent C_{dl} values.[33] This effect is reflected in the generally increasing C_{dl} values with increasing Ni concentration, with the exception of the 3.1% Ni sample, which exhibits the lowest capacitance. This decrease may be attributed to the strongly amorphous character of the coating and the higher surface roughness. Such structural features likely lead to a reduced number of exposed catalytic sites, hindered penetration of OH^- ions, and consequently inferior electrocatalytic performance. The 3.1% Ni sample also deviates from the general trend of decreasing charge-transfer resistance with increasing Ni concentration. While amorphous phases are often associated with a higher density of active sites due to structural defects and oxygen vacancies, they may also exhibit lower electrical conductivity due to the absence of long-range structural order.[22] In this case, the 3.1% Ni sample, characterized by a CP value of only 16.2%, appears to possess a less favorable electronic structure, resulting in slower electron transfer kinetics. Overall, the incorporation of Ni into the iron oxide structure is clearly beneficial, as it decreases R_{ct} values, thereby facilitating faster electron transfer and optimizing the adsorption energies of OER intermediates.

3.5. Long-Term OER Stability and Post-Test Characterization

The long-term electrocatalytic stability of the synthesized coatings was evaluated by chronopotentiometry in 1.0 M KOH at a constant current density of 10 mA·cm^{-2} for 50 h (Figure S8). All coatings exhibited great electrochemical stability, showing a slight activation during the initial stage of the measurement followed by a nearly constant potential throughout the remaining test period. After 50 h of continuous operation, all samples retained more than 99.5% of their initial potential, demonstrating high resistance to electrochemical degradation under OER conditions.

Although the chronopotentiometric measurements demonstrated excellent electrochemical stability over 50 h, the post-OER SEM observations (Figures S9 and S10) indicate that the most active coating (3.2 atom % Ni) undergoes noticeable morphological evolution under prolonged OER conditions. The pronounced surface deterioration, together with the measurable reduction in coating thickness observed by cross-sectional SEM, suggests that this composition is less resistant to the harsh alkaline environment and continuous oxygen evolution than coatings with lower Ni contents.[34] The higher catalytic activity of the 3.2 atom % Ni coating is accompanied by more intense oxygen evolution, which increases mechanical stresses associated with oxygen bubble nucleation and detachment and accelerates surface reconstruction and partial material loss. Consequently, although the catalyst maintains its electrochemical performance during the 50 h stability test, its morphology is less stable under prolonged operation in strongly alkaline electrolyte. The concurrent decrease in surface roughness after OER (Table S5) further indicates that unstable surface asperities were preferentially removed or reconstructed, resulting in a smoother but partially eroded surface.

The XPS results of post-OER samples (Table S3) revealed that after 50 h of electrochemical operation, the surface Fe^{2+} fraction increases markedly for every coating, reaching 77–84% at the expense of Fe^{3+}. Because Fe^{3+} is known to form soluble hydroxo/ferrate-type species under strongly alkaline conditions[35] and is therefore preferentially leached from oxide surfaces during prolonged anodic polarisation, this shift is consistent with selective dissolution of the outer, Fe^{3+}-enriched hematite/maghemite over-layer, which progressively exposes an underlying, more reduced Fe^{2+}-rich (magnetite-like) region. This interpretation is corroborated by two independent lines of evidence already reported: the measurable general corrosion currents obtained from Tafel extrapolation (Table 3) and the post-OER morphological degradation and coating-thickness reduction documented by SEM for the most active coating (Figures S9 and S10). The largest relative increase in Fe^{2+} content is observed for the film deposited at 60 W (4.6 atom % Ni, from 63.33 to 83.59%), suggesting that the highest-Ni coating is also the one whose outer oxidized layer is most susceptible to alkaline dissolution, even though this composition retains a low overpotential at 10 mA·cm^{-2}. Meanwhile, after 50 h of operation, the total surface Ni content changes only marginally for most compositions (e.g., 3.25 atom % before and after long-term OER at 40 W), indicating that the Fe^{2+}/Fe^{3+} and Ni^{2+}/Ni^{3+} redistributions discussed above reflect predominantly an internal re-speciation of the existing near-surface cations-consistent with preferential Fe^{3+} dissolution and Ni(II)/Ni(III) redox cycling rather than a net enrichment or depletion of nickel at the surface.

Electronic-structure considerations provide a further, complementary rationale for the absence of a simple, monotonic relationship between Ni content and OER activity (Figure 4,

https://doi.org/10.1021/acsaem.6c01330
ACS Appl. Energy Mater. XXXX, XXX, XXX–XXX

Table 2), in agreement with all results. Doping Fe-based oxides with Ni is widely reported to shift the Fe and Ni d-band centers in opposite directions, generally strengthening OH/O adsorption at Fe sites while weakening OOH binding at Ni sites, thereby producing a more balanced adsorption energetics across the four-electron OER pathway than either monometallic oxide alone. The present XPS results indicate that this electronic modulation is not fixed by composition alone but evolves with the specific phase assemblage and, upon operation, with Ni and Fe redox cycling; the coating exhibiting the most balanced Fe oxidation state and moderate crystallinity (3.2 atom % Ni) rather than the coating with the highest nominal Ni loading is the one that best approaches optimal adsorption energetics, consistent with the view that d-band and defect engineering, rather than dopant concentration per se, controls intrinsic activity in Ni-Fe oxide OER catalysts. The close numerical agreement between total surface Ni content (XPS) and bulk Ni content (EDS) at low-to-intermediate loading, together with the modest surface enrichment detected at the two highest nickel-target powers, is consistent with the general expectation that dopant segregation toward the surface of sputter-deposited oxide films becomes more pronounced as the nominal dopant loading increases and the host lattice becomes progressively more disordered. The essentially unchanged total surface Ni content before and after 50 h of operation, despite substantial internal Fe^{2+}/Fe^{3+} and Ni^{2+}/Ni^{3+} redistribution, further supports the conclusion that the observed OER performance differences originate from the specific oxidation-state balance and phase coexistence at the near-surface region rather than from bulk-to-surface nickel migration during operation.

4. CONCLUSIONS

Nickel-doped iron oxide coatings were synthesized in this work by reactive magnetron sputtering, with the Ni content controlled by varying the Ni target power between 25 and 60 W. Structural characterizations revealed that the applied target power governs not only the nickel concentration but also strongly influences the crystallinity and phase composition of the deposited films. Increasing the Ni target power, and consequently the Ni content, promotes the formation of increasingly amorphous coatings. Concurrently, the reactions occurring during deposition transform the initial hematite phase, enabling the formation of spinel-type phases such as Fe_3O_4, γ-Fe_2O_3, and $NiFe_2O_4$, characterized by different arrangements of Fe, Ni, and oxygen as well as the presence of oxygen vacancies.

In addition, within the Ni target power range of 30–40 W, an imbalance between the formation of an insulating oxide layer on the target surface and its removal during Ar^+ ion bombardment appears to favor the development of structurally disordered and non-equilibrium coatings, which correlates with reduced electrocatalytic performance. Although no direct correlation between dopant concentration and OER activity was observed, the results indicate that the synergistic interaction among the three iron oxide phases—hexagonal hematite and the spinel phases magnetite and maghemite—likely determines the optimal balance between amorphous and crystalline domains. This balance enhances the density of active sites and oxygen vacancies while maintaining sufficient electrical conductivity, thereby contributing to lower reaction overpotential, improved stability, and enhanced corrosion resistance in strongly alkaline electrolyte. Reactive-sputtering-controlled Fe^{2+}/Fe^{3+} disproportionation, composition-dependent Ni^{2+}/Ni^{3+} speciation reflecting competing substitutional and spinel-lattice incorporation pathways, a hydroxylated and defective rather than strictly oxygen-vacancy-rich surface, and an operationally reversible Fe- and Ni-redox surface reconstruction together provide a mechanistically coherent explanation for why the OER activity of these coatings tracks phase composition and its evolution under operating conditions rather than nickel concentration in isolation.

Comparison of the electrocatalytic performance of the coatings shows that the lowest overpotential (349.7 mV at 10 $mA{\cdot}cm^{-2}$) is achieved for films containing all three iron oxide phases, while the corresponding nickel concentration remains relatively lower, in the range of 2.6–4.6 atom %.

■ ASSOCIATED CONTENT

Supporting Information

The Supporting Information is available free of charge at https://pubs.acs.org/doi/10.1021/acsaem.6c01330.

Additional SEM images of the samples and figures illustrating the results of chronoamperometry, chronopotentiometry, and Tafel plots of corrosion measurements (PDF)

■ AUTHOR INFORMATION

Corresponding Author

Ieva Barauskiene – *Department of Physical and Inorganic Chemistry, Kaunas University of Technology, Radvilėnų str. 19, Kaunas 50254, Lithuania; Department of Physics, Kaunas University of Technology, Studentų str. 50, Kaunas 51368, Lithuania;* orcid.org/0000-0002-1027-7658; Email: ieva.barauskiene@ktu.lt.

Authors

Alexandre C. Bastos – *Department of Materials and Ceramic Engineering, CICECO-Aveiro Institute of Materials, University of Aveiro, Campus Universitário de Santiago, Aveiro 3810-193, Portugal;* orcid.org/0000-0003-1847-2332

Filipe M. L. Figueiredo – *Department of Physics, CICECO-Aveiro Institute of Materials, University of Aveiro, Campus Universitário de Santiago, Aveiro 3810-193, Portugal;* orcid.org/0000-0001-7799-2608

Giedrius Laukaitis – *Department of Physics, Kaunas University of Technology, Studentų str. 50, Kaunas 51368, Lithuania*

Complete contact information is available at: https://pubs.acs.org/doi/10.1021/acsaem.6c01330

Author Contributions

The manuscript was written through the contributions of all authors. All authors have given approval to the final version of the manuscript.

Funding

This work was supported by the Research Council of Lithuania (LMTLT) [grant number P-MIP-24-237]. This work was also developed within the scope of the project CICECO-Aveiro Institute of Materials, UIDB/50011/2020, UIDP/50011/2025, and LA/P/0006/2020, financed by national funds through the FCT/MCTES (PIDDAC).

Notes

The authors declare no competing financial interest.

REFERENCES

(1) United Nations Department of Economic and Social Affairs. *The Sustainable Development Goals Report 2025*; United Nations: New York, **2025**.

(2) Cárdenas Rodríguez, M.; Schwentner, E.; Falchi, E.; Suchodolski, A.; Pizarro, R. *National Greenhouse Gas Emission Inventories, Filling the Gaps in Official Data*; OECD Environment Working Papers 252; OECD Publishing: Paris, **2024**.

(3) Miller, H. A.; Bouzek, K.; Hnat, J.; Loos, S.; Bernäcker, C. I.; Weißgärber, T.; Röntzsch, L.; Meier-Haack, J. Green Hydrogen from Anion Exchange Membrane Water Electrolysis: A Review of Recent Developments in Critical Materials and Operating Conditions. *Sustain. Energy Fuels* **2020**, *4* (5), 2114–2133.

(4) Hu, C.; Zhang, L.; Gong, J. Recent Progress Made in the Mechanism Comprehension and Design of Electrocatalysts for Alkaline Water Splitting. *Energy Environ. Sci.* **2019**, *12* (9), 2620–2645.

(5) Santoro, C.; Lavacchi, A.; Mustarelli, P.; Di Noto, V.; Elbaz, L.; Dekel, D. R.; Jaouen, F. What Is Next in Anion-Exchange Membrane Water Electrolyzers? Bottlenecks, Benefits, and Future. *ChemSusChem* **2022**, *15* (8), No. e202200027.

(6) Li, H.; Han, X.; Zhao, W.; Azhar, A.; Jeong, S.; Jeong, D.; Na, J.; Wang, S.; Yu, J.; Yamauchi, Y. Electrochemical Preparation of Nano/Micron Structure Transition Metal-Based Catalysts for the Oxygen Evolution Reaction. *Mater. Horiz.* **2022**, *9* (7), 1788–1824.

(7) Xue, Y.; Sun, S.; Wang, Q.; Dong, Z.; Liu, Z. Transition Metal Oxide-Based Oxygen Reduction Reaction Electrocatalysts for Energy Conversion Systems with Aqueous Electrolytes. *J. Mater. Chem. A* **2018**, *6* (23), 10595–10626.

(8) Al-Naggar, A. H.; Shinde, N. M.; Kim, J. S.; Mane, R. S. Water Splitting Performance of Metal and Non-Metal-Doped Transition Metal Oxide Electrocatalysts. *Coord. Chem. Rev.* **2023**, *474*, No. 214864.

(9) Trześniewski, B. J.; Diaz-Morales, O.; Vermaas, D. A.; Longo, A.; Bras, W.; Koper, M. T. M.; Smith, W. A. In Situ Observation of Active Oxygen Species in Fe-Containing Ni-Based Oxygen Evolution Catalysts: The Effect of PH on Electrochemical Activity. *J. Am. Chem. Soc.* **2015**, *137* (48), 15112–15121.

(10) Espinosa, R. B.; Duits, M. H. G.; Wijnperle, D.; Mugele, F.; Lefferts, L. Bubble Formation in Catalyst Pores; Curse or Blessing? *React. Chem. Eng.* **2018**, *3* (5), 826–833.

(11) Barauskienė, I.; Blach, J.-F.; Saitzek, S.; Rousseau, J.; Mathieu, C.; Pakštas, V.; Valatka, E.; Laukaitis, G. Evaluation of Iron Oxide Coatings as Electrocatalysts for Oxygen Evolution Reaction Obtained via Electrodeposition and Magnetron Sputtering. *Appl. Surf. Sci.* **2025**, *690*, No. 162576.

(12) Orazem, M. E.; Tribollet, B. Assessing Regression Quality. In *Electrochemical Impedance Spectroscopy*; John and Wiley Sons, Inc.: Hoboken, NJ, **2008**; 385–403.

(13) Brug, G. J.; van den Eeden, A. L. G.; Sluyters-Rehbach, M.; Sluyters, J. H. The Analysis of Electrode Impedances Complicated by the Presence of a Constant Phase Element. *J. Electroanal. Chem. Interfacial Electrochem.* **1984**, *176* (1), 275–295.

(14) Hirschorn, B.; Orazem, M. E.; Tribollet, B.; Vivier, V.; Frateur, I.; Musiani, M. Determination of Effective Capacitance and Film Thickness from Constant-Phase-Element Parameters. *Electrochim. Acta* **2010**, *55* (21), 6218–6227.

(15) Martínez-Hincapié, R.; Wegner, J.; Anwar, M. U.; Raza-Khan, A.; Franzka, S.; Kleszczynski, S.; Čolić, V. The Determination of the Electrochemically Active Surface Area and Its Effects on the Electrocatalytic Properties of Structured Nickel Electrodes Produced by Additive Manufacturing. *Electrochim. Acta* **2024**, *476*, No. 143663.

(16) Connor, P.; Schuch, J.; Kaiser, B.; Jaegermann, W. The Determination of Electrochemical Active Surface Area and Specific Capacity Revisited for the System MnO_x as an Oxygen Evolution Catalyst. *Z. Phys. Chem.* **2020**, *234* (5), 979–994.

(17) Khatami, Z.; Wolz, L.; Wojcik, J.; Mascher, P. A Comprehensive Calibration of Integrated Magnetron Sputtering and Plasma Enhanced Chemical Vapor Deposition for Rare-Earth Doped Thin Films. *J. Mater. Res.* **2024**, *39* (1), 150–164.

(18) Sproul, W. D.; Christie, D. J.; Carter, D. C. Control of Reactive Sputtering Processes. *Thin Solid Films* **2005**, *491* (1), 1–17.

(19) Chamritski, I.; Burns, G. Infrared- and Raman-Active Phonons of Magnetite, Maghemite, and Hematite: A Computer Simulation and Spectroscopic Study. *J. Phys. Chem. B* **2005**, *109* (11), 4965–4968.

(20) Sedrati, C.; Alleg, S.; Boussafel, H.; Bendali Hacine, A. Structure and Magnetic Properties of Nickel Ferrites Synthesized by a Facile Co-Precipitation Method: Effect of the Fe/Ni Ratio. *J. Mater. Sci.: Mater. Electron.* **2021**, *32* (19), 24548–24559.

(21) de Souza, T. C.; Costa, A. F.; Vinhas, G. M.; Sarubbo, L. A. Synthesis of Iron Oxides and Influence on Final Sizes and Distribution in Bacterial Cellulose Applications. *Polymers* **2023**, *5*, 3284.

(22) Zhang, Y.; Gao, F.; Wang, D.; Li, Z.; Wang, X.; Wang, C.; Zhang, K.; Du, Y. Amorphous/Crystalline Heterostructure Transition-Metal-Based Catalysts for High-Performance Water Splitting. *Coord. Chem. Rev.* **2023**, *475*, No. 214916.

(23) Lu, D.; Yang, J.; Wang, X.; Gao, S.; Li, M.; Ji, H. Effect of Sputtering Power on the Microstructure and Properties of Silver Films Prepared by Magnetron Sputtering. *Mater. Today Commun.* **2025**, *42*, No. 111288.

(24) Messier, R.; Trolier-McKinstry, S. Thin-Film Processes. *In Encyclopedia of Materials: Science and Technology*; Buschow, K. H. J., Cahn, R. W., Flemings, M. C., Ilschner, B., Kramer, E. J., Mahajan, S., Veyssière, P., Eds.; Elsevier: Oxford, **2001**; pp 9306–9313.

(25) Biesinger, M. C.; Payne, B. P.; Grosvenor, A. P.; Lau, L. W. M.; Gerson, A. R.; Smart, R. S. C. Resolving Surface Chemical States in XPS Analysis of First Row Transition Metals, Oxides and Hydroxides: Cr, Mn, Fe, Co, and Ni. *Appl. Surf. Sci.* **2011**, *257* (7), 2717–2730.

(26) Bagus, P. S.; Nelin, C. J.; Brundle, C. R.; Lahiri, N.; Ilton, E. S.; Rosso, K. M. Analysis of the Fe 2p XPS for Hematite α Fe_2O_3: Consequences of Covalent Bonding and Orbital Splittings on Multiplet Splittings. *J. Chem. Phys.* **2020**, *152* (1), 14704.

(27) Idriss, H. On the Wrong Assignment of the XPS O1s Signal at 531–532 EV Attributed to Oxygen Vacancies in Photo- and Electro-Catalysts for Water Splitting and Other Materials Applications. *Surf. Sci.* **2021**, *712*, No. 121894.

(28) Easton, C. D.; Morgan, D. J. Critical Examination of the Use of X-Ray Photoelectron Spectroscopy (XPS) O 1s to Characterize Oxygen Vacancies in Catalytic Materials and Beyond. *J. Vac. Sci. Technol., A* **2025**, *43* (5), 53205.

(29) Wang, J.; Mueller, D. N.; Crumlin, E. J. Recommended Strategies for Quantifying Oxygen Vacancies with X-Ray Photoelectron Spectroscopy. *J. Eur. Ceram. Soc.* **2024**, *44* (15), No. 116709.

(30) Barauskienė, I.; Laukaitis, G.; Valatka, E. Stainless Steel as an Electrocatalyst for Overall Water Splitting under Alkaline and Neutral Conditions. *J. Electroanal. Chem.* **2023**, *950*, No. 117880.

(31) Hiromoto, S. Metals for Biomedical Devices. In *Metals for Biomedical Devices*; Niimomi, M., Ed.; Elsevier, **2019**; pp 99–121.

(32) Papavinasam, S. 3 - Electrochemical Polarization Techniques for Corrosion Monitoring. In *Woodhead Publishing Series in Metals and Surface Engineering*; Yang, L., Ed.; Woodhead Publishing, **2021**; pp 45–77.

(33) Duquesne, E.; Betelu, S.; Bazin, C.; Seron, A.; Ignatiadis, I.; Perrot, H.; Sel, O.; Debiemme-Chouvy, C. Insights into Redox Reactions and Ionic Transfers in Nickel/Iron Layered Double Hydroxide in Potassium Hydroxide. *J. Phys. Chem. C* **2020**, *124* (5), 3037–3049.

https://doi.org/10.1021/acsaem.6c01330
ACS Appl. Energy Mater. XXXX, XXX, XXX–XXX

(34) He, B.; Bai, F.; Jain, P.; Li, T. A Review of Surface Reconstruction and Transformation of 3d Transition-Metal (Oxy)Hydroxides and Spinel-Type Oxides during the Oxygen Evolution Reaction. *Small* **2025**, *21* (10), No. 2411479.
(35) Sipos, P., Zeller, D., Kuzmann, E., Vértes, A., Homonnay, Z., Walczak, M., & Canton, S. E. The structure of Fe(III) ions in strongly alkaline aqueous solutions from EXAFS and Mössbauer spectroscopy. *Dalton Trans.* **2008**, *7*(41), 5603–5611.

https://doi.org/10.1021/acsaem.6c01330
ACS Appl. Energy Mater. XXXX, XXX, XXX–XXX